Key Points:
- Tristatic observations with EISCAT VHF show for the first time wind shear in PMSE
- Observed wavy PMSE structure supports models that PMSE form due to Kelvin-Helmholtz instability caused by wind shear
- Electron density is for prolonged time reduced directly above PMSE, while it appears not perturbed at PMSE altitude

Correspondence to:
I. Mann,
ingrid.b.mann@uit.no

First wind shear observation in PMSE with the tristatic EISCAT VHF radar

I. Mann[1], I. Häggström[2], A. Tjulin[2], S. Rostami[3], C. C. Anyairo[3], and P. Dalin[4]

[1]Department of Physics and Technology, UiT the Artic University of Norway, Tromsø, Norway, [2]EISCAT Scientific Association, Kiruna, Sweden, [3]Space Technology Division, Luleå University of Technology, Luleå, Sweden, [4]Swedish Institute of Space Physics, IRF, Kiruna, Sweden

Abstract The Polar Summer Mesosphere has the lowest temperatures that occur in the entire Earth system. Water ice particles below the optically observable size range participate there in the formation of strong radar echoes (Polar Mesospheric Summer Echoes, PMSE). To study PMSE we carried out observations with the European Incoherent Scatter (EISCAT) VHF and EISCAT UHF radar simultaneously from a site near Tromsø (69.58°N, 19.2272°E) and observed VHF backscattering also with the EISCAT receivers in Kiruna (67.86°N, 20.44°E) and Sodankylä (67.36°N, 26.63°E). This is one of the first tristatic measurements with EISCAT VHF, and we therefore describe the observations and geometry in detail. We present observations made on 26 June 2013 from 7:00 to 13:00 h UT where we found similar PMSE patterns with all three VHF receivers and found signs of wind shear in PMSE. The observations suggest that the PMSE contains sublayers that move in different directions horizontally, and this points to Kelvin-Helmholtz instability possibly playing a role in PMSE formation. We find no signs of PMSE in the UHF data. The electron densities that we derive from observed incoherent scatter at UHF are at PMSE altitudes close to the noise level but possibly indicate reduced electron densities directly above the PMSE.

1. Introduction

Polar Mesospheric Summer Echoes (PMSE) are strong radar echoes caused by spatial variations in the plasma refractive index at around the 80 to 90 km altitude in the Earth's mesosphere [*Cho and Röttger*, 1997; *Chilson et al.*, 2000; *Rapp and Lübken*, 2004; *La Hoz et al.*, 2006]. PMSE arise in the presence of ice particles that carry an electric surface charge. They form when the temperature reaches its global minimum close to the mesopause during polar summer and occur in both hemispheres [see e.g., *Morris et al.*, 2007]. The water condenses onto nanometer-sized dust. The ice particles form polar mesospheric clouds (PMC) which can be observed from satellites [*Hervig et al.*, 2013]. Under certain conditions they are also visible from the ground in noctilucent clouds (NLC). Furthermore, rocket measurements prove that charged particles exist at the altitudes of PMC and NLC [*Havnes et al.*, 1996]. The dust/ice particles influence atmospheric chemistry [cf. *Plane et al.*, 2015]. In particular, the dust charges are an important parameter because they influence ice condensation [*Megner and Gumbel*, 2009] and chemical processes [*Baumann et al.*, 2015]. The charged ice particles that are below the optically observable size range are still observable through PMSE.

A possible variation in the abundance of ice particles and links to anthropogenic atmospheric changes are controversially discussed based on NLC observations that span over more than a century [*Thomas et al.*, 1989; *Gadsken*, 1990; *Thomas*, 2003; *von Zahn*, 2003]. Recent studies based on different observational results suggest a long-term increase of the mesospheric ice particles at high latitude [*DeLand and Thomas*, 2015] but an absence of statistically significant trends during the last 50 years at midlatitude [*Pertsev et al.*, 2014]. PMSE can be observed independently from weather conditions and provide information on the occurrence of ice particles that influence atmospheric chemistry, as well as on neutral dynamics. The atmosphere at PMSE altitude is influenced by solar radiative forcing from above and gravity waves from below, and while ionization is small, it is highly variable due to a number of different processes. Because PMSE are among the few examples of dusty plasma observed in nature [cf. *Mendis and Rosenberg*, 1994], the process of radio wave scattering that generates the PMSE is of interest for dusty plasma research. It is also of interest for observational studies because it also involves charged ice particles at the first stage of formation below the size of the optically observed particles [cf. *Rapp and Lübken*, 2009; *Varney et al.*, 2011]. All this makes PMSE an interesting object of observations, but to make full use of the observations improved understanding of PMSE is needed.

Table 1. Radar System Parameters

	Tromsø VHF	Kiruna VHF	Sodankylä VHF	Tromsø UHF
	Transmit/Receive	Receive	Receive	Transmit/Receive
Frequency	224.4 MHz	224.4 MHz	224.4 MHz	929.9 MHz
Wavelength	1.34 m	1.34 m	1.34 m	0.32 m
Transmitter peak power	1.5 MW			2 MW
Radar code	Manda[a]			Manda[a]
Resolution in range/time delay	360 m	360 m	360 m	360 m
System temperature	240–370[b] K	135 K	150 K	90–150 K
Antenna gain	43 dBi			48 dBi
Half-power beam width	$1 \times 2.4° \times 1.7°$ transmit	1.2°	1.2°	1.2°
	$2 \times 2.4° \times 1.7°$ receive			

[a]https://www.eiscat.se/about/experiments2/experiments.
[b]Includes additional noise from range-aliased F region echoes.

PMSE form because spatial irregularities in electron density cause enhanced scattering of radio waves, and the formation process involves neutral air turbulence and charged ice particles. Many initial theories regarding the formation of the scattering are based on applying a multipolar diffusion theory [*Hill*, 1978] to a system of electrons, positive ions, and charged aerosol/ice particles as first developed by *Cho et al.* [1992]. The presently widely accepted view is that neutral air turbulence in combination with reduced electron diffusivity is responsible for PMSE formation and charged heavy ice particles controlled by neutral air reduce the mobility of the free electrons that scatter the radio waves [*Rapp and Lübken*, 2004]. A straightforward quantitative description of the links between the parameters involved is, however, missing [cf. e.g., *Rapp and Lübken*, 2004; *La Hoz et al.*, 2006, and references therein]. Furthermore, there are indications that different PMSE processes exist, as, e.g., rocket observations have shown that turbulence was absent in 7 out of 10 observed PMSE layers [*Lübken et al.*, 2002].

In view of the large number of unknowns, any new observation and novel approaches are of interest. We here present one of the first tristatic PMSE observations where the radio waves were transmitted vertically and PMSE were observed from the transmit antenna as well as two distant receiver antennas, that is, were observed vertically and at slant view. We first describe in detail the observation geometry and analysis in section 2 because we are not aware of any previous presentations of this. We then present the observational results in section 3 and describe the horizontal motion that we find in the PMSE. In section 4 we discuss the observational results and suggest that they indicate that possibly Kelvin-Helmholtz instability plays a role in the PMSE formation. We also show that for the atmospheric parameters at the time of the observations it is possible that Kelvin-Helmholtz instability occurs. Because this is of interest for the planning of future observation campaigns we also discuss the results of measured incoherent scatter observations although they are close to detection limit. We end the paper with a remark on future observations (section 5) where we point out the improvement in measurement capabilities that will be achieved with future multistatic phased-array radar studies of PMSE.

2. Observation and Analysis

The observations were made on 26 June 2013 from 7:00 to 13:00 h UT. The radar signal was transmitted in zenith direction with the European Incoherent Scatter (EISCAT) VHF (224 MHz) and UHF (929 MHz) antennas near Tromsø (69.59°N, 19.23°E), and the backscattered signal was measured with the same antennas, which is the routine configuration for PMSE observations. In addition, the EISCAT VHF remote receiver antennas were pointed toward Tromsø so that their sight lines crossed the illuminating beam at the altitude where PMSE occur. The remote receivers in this tristatic configuration are located in Kiruna (67.86°N, 20.44°E) and Sodankylä (67.36°N, 26.63°E) at a distance 199 km and 391 km from the transmit antenna, respectively. The radar code used was Manda, and references to EISCAT documentation and radar system parameters are given in Table 1. The sight lines of the remote receiver antennas subsequently pointed at heights, H_P (reference heights), of 86, 90, 94, 82, 86, and 84 km above the Tromsø site (in this sequence). The antenna elevations that correspond to those reference heights are listed in Table 2.

Table 2. Antenna Elevation Angles and Beam Dimensions

H_P (km)	82	84	86	90	94
			Kiruna Antenna		
Elevation	21.30°	21.78°	22.28°	23.24°	24.17°
H_{max} (km)	95	96	99	103	107
H_{min} (km)	66	69	70	75	79
			Sodankylä Antenna		
Elevation	9.96°	10.23°	10.57°	11.05°	11.61°
H_{max} (km)	96	97	101	104	108
H_{min} (km)	65	68	68	73	78

We first discuss the geometry of the tristatic EISCAT VHF and the measurements with the remote receivers. Figure 1 sketches in a vertical cut the geometry of the transmit antenna pointing toward zenith and remote receiver antennas pointing at a reference height at point V above the transmit antenna; it also illustrates the large range of altitude over which the remote receivers measure the backscattered signal. The minimum altitudes, H_{min}, and maximum altitudes, H_{max}, where the antenna beams cross the illuminated volume are listed in Table 2 (numbers rounded to kilometers). The data received at one point in time from Kiruna and Sodankylä as displayed by EISCAT real-time graph (RTG) are shown in Figure 2. The postexperiment integration time of displayed data is 19.2 s. The frames in the right column show frequency shift relative to the transmitted frequency, f_0 set to $f_0 = 0$ (in figures) on the abscissa and signal time delay, τ, on the ordinate. The signal time delays corresponding to the path length along the antenna sight lines are set to $\tau_0 = 0$. In the case of the Kiruna antenna this is the length Δ (T,V,K) of the line from T through V to K (cf. Figure 1). The signals received with time delay τ_0 do not only scatter from V but are collected from any point P in the volume which connects to T and K to the same total length as V does. These points P describe a segment of a circle within the vertical cut of volume shown, and signals with $\tau < 0$ are from the part of the illuminated volume below this line and those with $\tau > 0$ from part of the volume above. The data are recorded in 2.4 µs time delay intervals corresponding to 360 m range interval, and a total of 53 subvolumes (of the beams intersection volume) is measured. The same applies for the Sodankylä measurements. Power versus time delay is shown in Figure 2 (left column), where also the (low) power received from outside the considered frequency interval can be seen for comparison.

The selected frequency interval of the power versus frequency frames (Figure 2, right column) of ±100 Hz around the transmit frequency corresponds to the approximate expected width of incoherent scatter spectra at 80 to 90 km altitude [cf. *Röttger and LaHoz*, 1990]. The spectra displayed in the frames have a width around 20 Hz or less which indicates they are not from incoherent scatter but coherent scattering from PMSE. The shift of frequency is Doppler shift due to motion of the scattering obstacle along the sight line. It is also apparent from the frames that this frequency shift is different for different time delays, and namely, in the frame describing Kiruna measurements (Figure 2, right column, lower panel) the power is distributed at frequencies $< f_0$ for $\tau < \tau_0$ and at frequencies $> f_0$ at $\tau > \tau_0$, approximately indicating that the observed volume in space includes scattering obstacles with different direction of motion along the sight line. The same frame shows that spectral power distributions at given time delay have only one peak. We observe this in the data in general. For
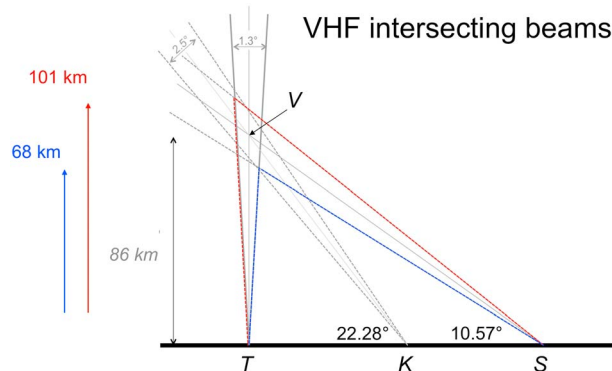

Figure 1. Geometry of receiver antenna cones crossing illuminated volume above Tromsø showing both receiver sight lines projected onto same vertical plane. The antenna sight lines intersect at point V and originate from points T, K, S for Tromsø, Kiruna, and Sodankylä, respectively. Scattered components are received from any point P within the overlapping volume. For antenna pointing at 86 km the maximum and minimum heights observed from Sodankylä are given.
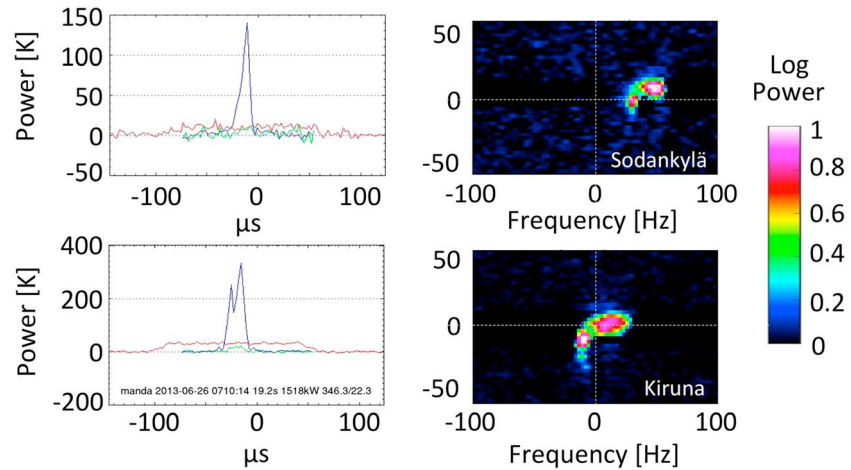
Figure 2. The 7:10 UT data from EISCAT real-time graph (RTG) for Kiruna and Sodankylä receivers. (left column) Blue lines describe as function of time delay the received power, given relative to system temperature. Red and green lines describe undeconvoluted power in considered spectral interval and power outside this interval, respectively. (right column) For same data the power distribution versus frequency on the abscissa within considered ±50 Hz interval around transmit frequency (set to zero) and time delay in μs on ordinate. Color codes describe backscattered power relative to maximum received power within each frame.

the same data, total backscattered power (in the entire frequency interval) as function of time delay (Figure 2, left column, lower panel) shows two peaks. Our interpretation of this observation is that the upper part of observed volume contains a component that moves away from the receiver antenna and the lower part a component that moves toward the receiver antenna.

In Figure 3 a number of frames of observations from all three antennas are displayed. Each panel presents measurements from one site in the same way as in Figure 2 discussed above. Tromsø frames show altitude derived from pulse time delay on the ordinate (instead of time delay). One of the frames shows high background noise level due to the influence of other radar signals, e.g., from airplane crossing in a sidelobe of one or both radar beams (see Sodankylä 8:30 UT). One can see that the echoes are observed from all sites at similar altitude, and sometimes two separate peaks can be seen in the power distribution, like at 8:30 UT. The displayed Kiruna and Sodankylä data from 9:30 UT nicely show frequency shift around τ_0 which indicates that the direction of motion changes over height smaller than one range interval. The patterns in Figure 3 result from layers within the PMSE because they appear in subsequent frames. This can also be seen when considering the measurements taken over time.

To obtain the PMSE observed over time with the remote receivers, we derive from each time frame the total backscattered power, the width of its frequency distribution, and its frequency shift compared to the transmission frequency. Since the radar path of the remote receivers includes a vertical and a horizontal component within a large beam volume, a conversion to altitudes is not meaningful.

For data from the Kiruna and Sodankylä remote receivers we describe the power as function of frequency with a single Gaussian profile to derive the power amplitude and the width and shift of the frequency distribution. We note that the spectral distributions in our data are broader than those that other groups derived from monostatic observations [e.g., *Strelnikova and Rapp*, 2011; *Belova et al.,* 2014]. We see no apparent overlap of several lines in the profiles but assume that the broad distribution is due to the signal being integrated over large volume. We here use the Gauss fit merely to estimate the overall width and shifts of the distributions. When considering for comparison the mean value of the power versus frequency distribution we obtained an overall similar result (not shown). The observed frequency shifts are due to Doppler shift caused by motion of the scattering atmospheric compounds along the sight line. The frequency converts to line-of-sight velocities with

$$\Delta v = \Delta\omega \ \lambda/4 \ \pi \ \sin(\varphi/2) \tag{1}$$

where $\Delta\omega = 2 \pi \Delta f$, $\lambda = c/f$, and φ is the scattering angle. The widths of the spectral distributions observed are similar for Kiruna and Sodankylä and typically within 20 Hz; they are of the same order as the observed
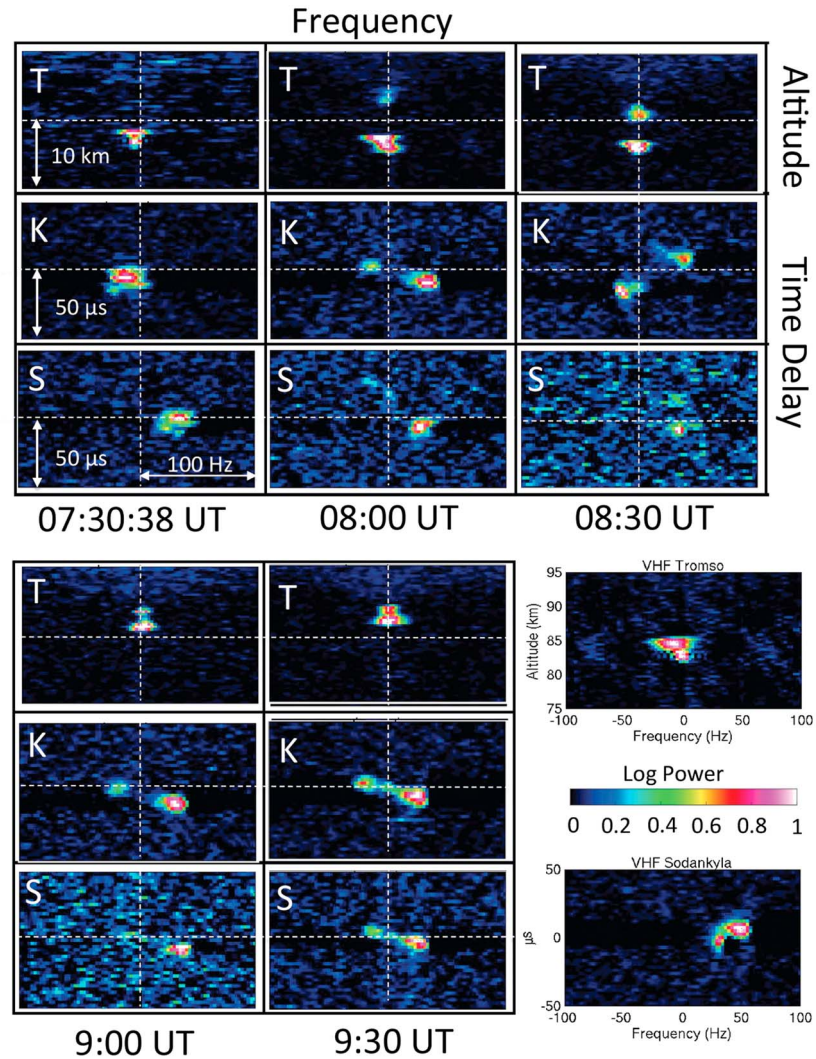
Figure 3. Individual frames of the VHF observations are shown in three panels for Tromsø, Kiruna, and Sodankylä. Each frame shows frequency shift relative to the transmitted pulse on the abscissa. The signal time delay is given on the ordinate, for Tromsø this is directly converted to altitude. The color code describes the backscattered power, normalized to maximum received power within each frame. Scales and legends given in the lower right of the figure are valid for all frames from the same cite, and those for Sodankylä also apply to the Kiruna observations.

frequency shifts. We presume they result from the different velocity components observed within the large beam volumes and will not discuss them further. Because of this, we also do not study in detail here the spectral shape as was done in a study of monostatic observations [cf. *Strelnikova and Rapp*, 2010]. The pointing of the remote receiver antennas was changed during the measurements. The change of pointing within ≈ minute had an influence on the time delay distribution in the individual frames (like those displayed in Figures 2 and 3) but not on the spectral distribution. There is not apparent influence on the overall observed PMSE patterns presented and discussed below.

At altitudes without PMSE and where ionization is sufficiently high EISCAT measures the incoherent scatter from electrons. This signal is at 80 to 100 km much fainter and covers a broader frequency distribution than PMSE [cf. *Cho and Röttger*, 1997; *Rapp and Lübken*, 2004; *La Hoz et al.*, 2006]. For, otherwise, analyzing the VHF and UHF Tromsø measurements we used standard incoherent scatter analysis GUISDAP [*Lehtinen and Huuskonen*, 1996]. GUISDAP provides the electron density derived from the incoherent scatter spectrum and a value proportional to backscattering power for the coherent scatter of the PMSE. Considering, e.g., the spectral distributions in VHF Tromsø measurements shown in Figure 3, there is no incoherent scatter
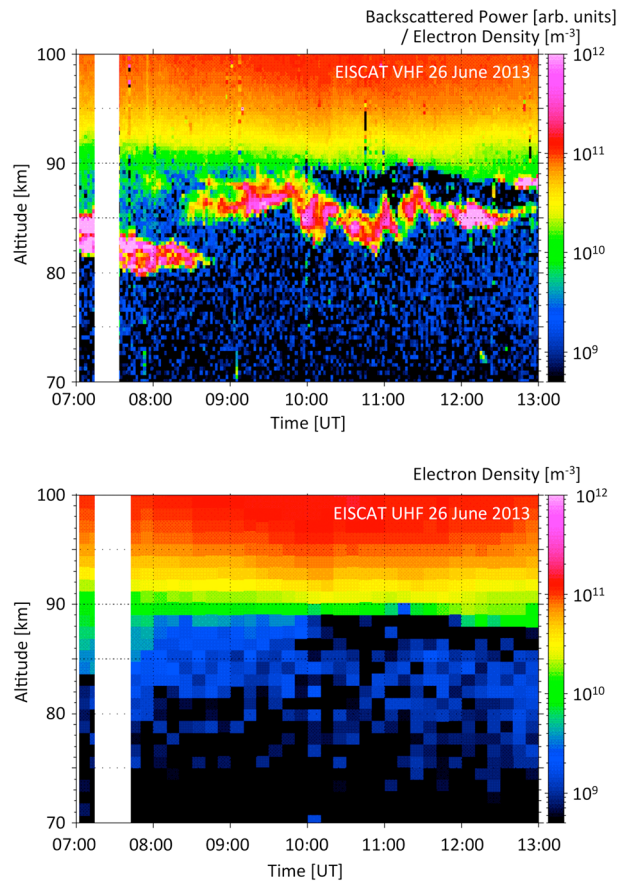
Figure 4. The radar backscattered power and electron density observed with EISCAT (top) VHF and (bottom) UHF during 6 h at altitudes given on the ordinate. A data gap occurs because of a reception problem starting 7:14 UT, left blank in the figures. No PMSE is observed with UHF, and measured electron densities are plotted with 10 min postexperiment integration time for illustration of small electron densities.

component noticeable at the PMSE altitudes. From the VHF observations we also derive the vertical velocity in the PMSE discussed below from the mean Doppler shift of the backscattered signal as described, e.g., by *Strelnikova and Rapp* [2011].

3. Results

Figure 4 presents the Tromsö VHF and UHF measurements, and Figure 5 describes the VHF measurements from the remote sites. All VHF measurements show PMSE over the entire 6 h time interval at varying altitude between 80 and 90 km, and the appearance is remarkably similar in observations from all three sites. The UHF measurements can be explained as incoherent scatter; they show no apparent PMSE, which is in line with findings that PMSE are rarely observed at higher frequency and occurrence rate is much lower for EISCAT UHF than for VHF [*La Hoz et al.,* 2006; *Strelnikova and Rapp*, 2011]. In some parts of the PMSE a wave-like patterns can be seen. Those are often observed in PMSE similar as in NLC and are possibly due to gravity waves that cause turbulence in the neutral component [*Dalin et al.,* 2012]. We find that changing the elevation of the remote receiver antennas had no noticeable influence on the observed overall spatial structure
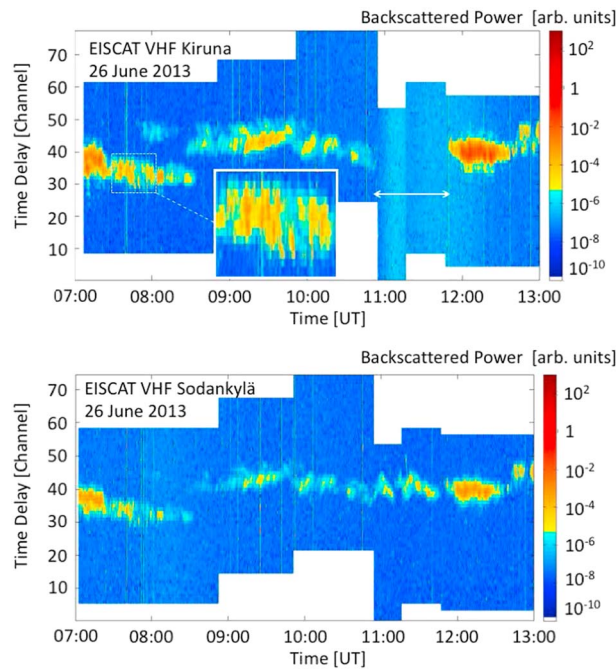
of PMSE, and we assume this is because the resulting change in observation geometry is small compared to the size of the observed volume. As seen in Figure 3 the frequency shift sometimes changes at a given time along the antenna sight lines. Figure 6 shows the frequency shifts observed during the entire observation run showing that at a given altitude similar frequency shifts are observed for some (prolonged) time suggesting they are due to wind motion. The observed frequency shifts are within ±30 Hz and for most of the time clearly different for Kiruna and Sodankylä data indicating the contribution from horizontal components. During some time intervals the measurements include a reversal in the frequency shift with altitude. In this tristatic observation geometry sight lines of the remote receivers have a large horizontal component, and reversals can be seen when the sight line crosses layers with different directions of motion, as illustrated in Figure 7.

The overall direction of motion in the presented observations can be estimated from the combination of frequency shifts that are observed from Sodankylä and Kiruna, respectively, as sketched in Figure 7 applying that positive frequency shift along the sight line is generated from objects moving toward and negative shift from objects moving away from the receiver along the sight line. Combination of the shift along the two different sight lines (for Kiruna and Sodankylä observations) provides a rough estimate of the direction of motion. From that the reversal in motion around 7:15 UT is from overall eastward motion in the upper layer to northward in the lower layer, while around 9:15 UT the upper layer moves north and the lower layer east. Around 12:00 UT motions are toward west in the upper layer and north in the lower layer with northward motion at all altitudes around 12:15 UT and later. The vertical motion derived from the Tromsø observations, displayed in Figure 8, is in comparison small and does not show any evidence for the sublayers that we infer

Figure 5. The radar backscattered power measured from the VHF remote receivers in (top) Kiruna and (bottom) Sodankylä as function of signal time delay. Different observation time intervals were shifted so that a horizontal line within each figure corresponds to same altitudes above Tromsø. The display of data from the lowest pointing (82 km) starts at channel 0, the measurements pointing to reference height 84, 86, 90, and 94 km are shifted by 4, 8, 16, and 24 channels for the Kiruna data and by 3, 5, 14, and 21 channels for the Sodankylä data, respectively. A timing problem at the Kiruna site resulted in a data gap from 10:54 UT to 11:50 UT, marked with an arrow. The white rectangular marks a wavy structure in the PMSE pattern that is discussed in the text.

from the observations with the remote receivers. The derived vertical velocities are around m/s, and variation in vertical velocity is larger outside of the PMSE; the latter was also noted by other observers [cf. *Strelnikova and Rapp*, 2011].

4. Discussion

The patterns of PMSE that we observed from the three different sites appear similar. During the observations we changed several times the pointing directions of the receiver antennas and found no noticeable effect on the observed backscattered power, so there is no sensitivity on aspect angle within the limits of the presented observations with elevation angles 21.30° to 24.17° and 9.96° to 11.61° (cf. Table 2). In general, the changes of pointing direction had little influence on the observations. We explain this with the large extension of the volume that the antenna beams cover, with the large overlap of the beams with different antenna pointings, and with the fact that the observed signals typically come from the part in the antenna volume where reflectivity is highest. We suggest that different types of radar systems are needed for a detailed study of aspect sensitivity. At

the same time we can derive from the observations important information on the horizontal layering of the PMSE. The small vertical velocities that we derive from the Tromø observations are an important indicator that the Doppler shifts observed with the remote receiver antennas are due to horizontal motion. These fre-
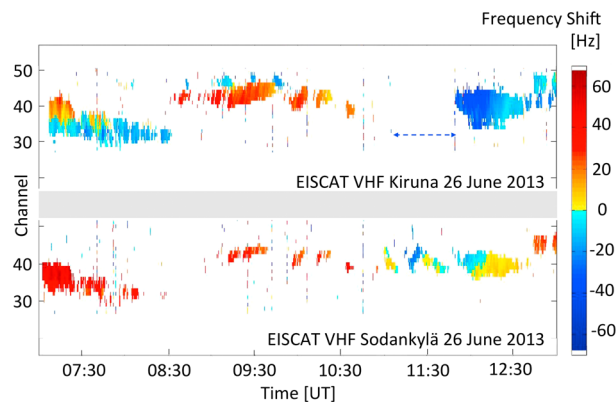

Figure 6. The frequency shift of the backscattered power measured from (top) Kiruna and (bottom) Sodankylä. The channels were shifted in the same way as in Figure 5. A change of the direction of frequency shift with height is best seen in the Kiruna data between 7:10 to 7:40 and 9:00 to 10:00 UT.

quency shifts and their implications for layers in the PMSE, as well as the results on incoherent scatter, are discussed in more detail below.

4.1. Frequency Shift and PMSE Layers

We interpret the observed reversal in frequency shift as due to wind shear and suggest that Kelvin-Helmholtz instability can evolve. A wavy structure of the boundary is a characteristic of Kelvin-Helmholtz instability, and such signatures can be seen in the backscattered power and in the frequency shift of the Kiruna measurements between 07:10 and 07:40 UT (cf. Figures 5 and 6). While this needs to be supported with future observations, the interpretation is plausible also based on
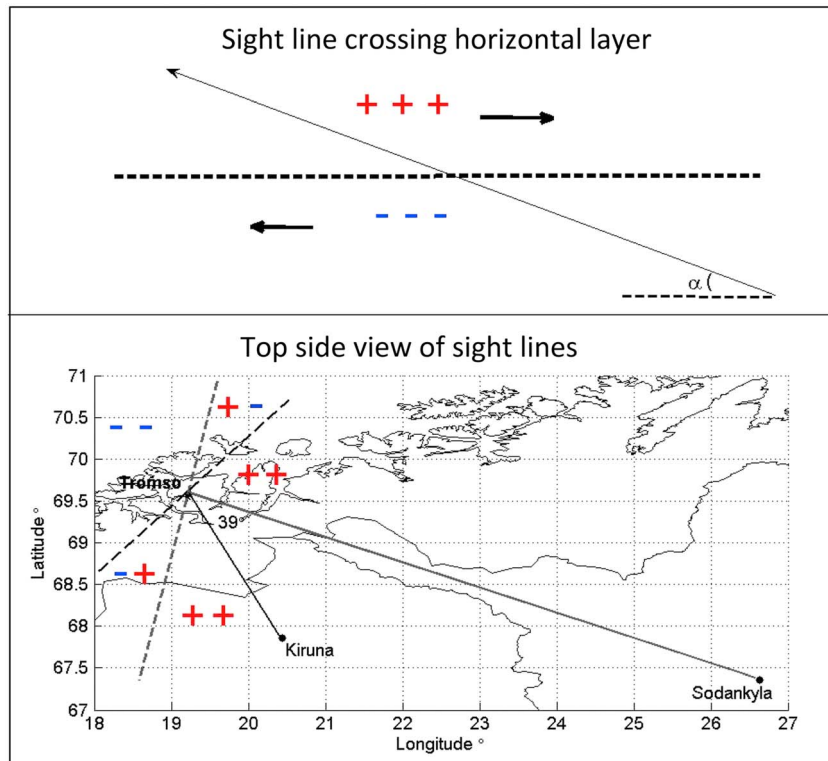
Figure 7. (top) Geometry of observation showing in vertical cut through the atmosphere how the antenna sight lines cross layers with different directions of motion. (bottom) The observation geometry shows the direction of the sight line projection from the illuminated volume above Tromsø to the receiver antennas. The dashed lines separate directions of motion with positive (to the right) and negative (to the left) frequency shifts. The overall direction of motion can be estimated from the combination of frequency shifts that are observed from, respectively, Sodankylä and Kiruna where positive/negative indicated overall northward motion; negative/negative, westward; negative/positive, southward; and positive/positive, eastward as sketched in the figure.

considering the Richardson number, given as the ratio of the squared Brunt-Väisälä frequency to the squared horizontal wind gradient. Assuming a typical Brunt-Väisälä period at the summer mesopause of 5 min [*Andrews et al.,* 1987] and horizontal wind gradient of 20 m/s over few hundred meters height, we obtain a Richardson number around 0.2 while instabilities are expected for Richardson numbers smaller than 0.25 [*Fritts and Alexander*, 2003]. The observed shape of PMSE also suggests its link turbulence. *Varney et al.* [2011] show that PMSE reflectivity dependents, among others, on the number density of charged ice particles and on their height gradient, Brunt-Väisälä frequency, and turbulent energy dissipation rate. *Dalin et al.* [2012] have checked these equations using real atmospheric data inside the PMSE layer and found that indeed the variability in the PMSE reflectivity is readily explained by the ice number density, its height gradient, and wave-induced perturbations in the buoyancy period and the turbulent energy dissipation rate.
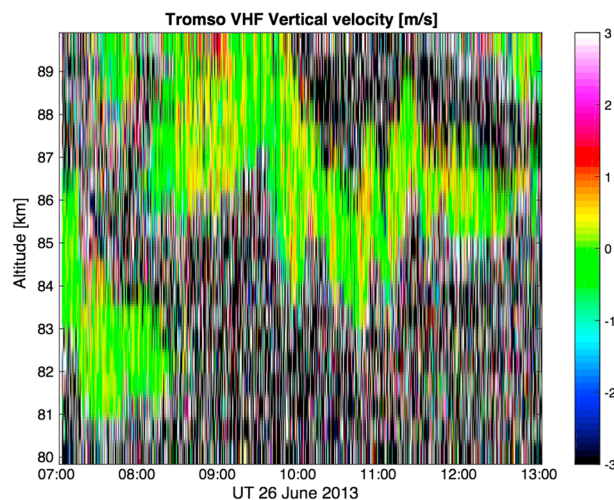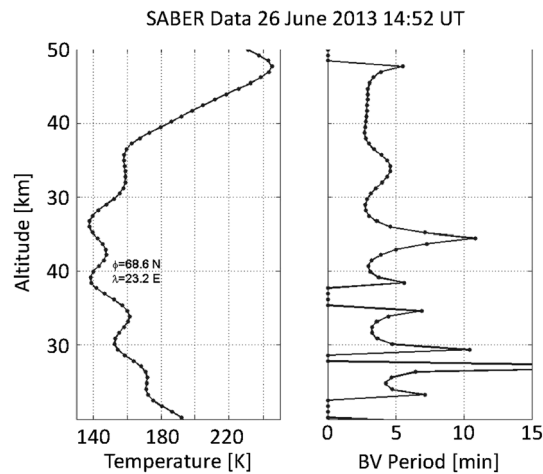

Figure 8. The vertical velocity derived from frequency shift of backscattered power in the EISCAT VHF observations displayed in Figure 4. Velocities are within ±1 m/s in PMSE signals and larger otherwise.

Figure 9. (left) Temperature profile and (right) Brunt-Väisälä (BV) period calculated based on this temperature profile from SABER measurements [*Russell et al.*, 1999] on board TIMED [cf. *Remsberg et al.*, 2008]. This temperature profile from SABER at distance 217 km from the Tromsø EISCAT site is the closest in space and time to the period and location of the PMSE observations.

To further explore that Kelvin-Helmholtz instability formation is plausible, we refer to an observed vertical temperature profile taken the same day 217 km away from the Tromsø site. The temperature profile and the Brunt-Väisälä period derived from it are shown in Figure 9. The temperature measurements are from the infrared radiometer SABER (Sounding of the Atmosphere using Broadband Emission Radiometry, [*Russell et al.*, 1999]) on board the TIMED (Thermosphere Ionosphere Mesosphere Energetics and Dynamics) satellite. The validation of the SABER temperature data can be found in *Remsberg et al.* [2008, and reference therein]. We have selected the temperature profile closest in space and time to the Tromso position during the period of the PMSE observation. The Brunt-Väisälä period goes to imaginary values (zeros in Figure 9) which is a strong indication for the presence of the convective instability. While this observation is not from the same volume as the PMSE observations, it indicates the possible existence of Kelvin-Helmholtz instability at locations and for mesospheric conditions very close to the EISCAT observations.

We note that *Yu et al.* [2001] with coherent radar imaging also find horizontal structure in PMSE reflectivity and velocity in PMSE multiple layers and suggest Kelvin-Helmholtz instability one possible explanation. Kelvin-Helmholtz instability caused by wind shears is also observed in NLC [*Dalin et al.*, 2010]. In addition to the observational findings, also hydrodynamic models show that turbulence can initiate Kelvin-Helmholtz instability and lead to strong radar echoes from electron irregularities in the presence of heavy ions and charged dust [*Hill et al.*, 1999]. It is also worthwhile to note that in other atmospheric studies, the influence of wind shear is observed even at higher altitude, e.g., at sporadic *E* layers [*Hysell et al.*, 2014].

The observation of high horizontal velocity components also has an implication for the link between PMSE and NLC. In general, the peak of PMSE detections is around 86 km and the peak of NLC occurrence is around 83 km, and this suggests the picture of ice particles that grow, settle, and sublimate in the mesosphere and gives rise to both phenomena [cf. *Rapp and Lübken*, 2004]. The observed horizontal motion of the PMSE in different directions may imply sharp changes in the ice number density and its height gradient. Both are found to be significant factors in the variability of the PMSE reflectivity [*Varney et al.*, 2011; *Dalin et al.*, 2012]; however, these factors may have different influence on the larger NLC ice particles at lower altitude. In the first common volume and simultaneous NLC and PMSE observations with LIDAR from ALOMAR *Nussbaumer et al.* [1996] observed PMSE every day for 1 month (23 July to 23 August 1994), while simultaneous NLC/PMSE events were only observed in four cases—partly because of weather conditions. From a campaign using visual observations and photography together with radar at ESRANGE and EISCAT *Kirkwood et al.* [1995] could not find a correlation between NLC and PMSE because there were only few cases of common volume observations. This latter campaign was carried out during summer 1991.

4.2. Electron Densities

The altitude and radar frequencies at which PMSE are observed suggest that they are linked to charged dust/ice particles [*Rapp and Lübken*, 2004] and they are even considered a dusty plasma [*Mendis and Rosenberg*, 1994]. Some models are, e.g., based on the assumption that charged dust particles are carried with the neutral atmosphere so that they form an irregular spatial pattern. To satisfy the charge neutrality

condition, the charged dust distribution causes electron density variation and that, in turn, changes the index of refraction so that the radar echoes form. The index of refraction, ε, here is at (angular) frequency ω

$$\varepsilon = \left(1 - \omega^2/\omega_p{}^2\right) \qquad (2)$$

with the plasma frequency $\omega_p \approx (n_e e^2/\varepsilon_o m_e)^{1/2}$, electron density n_e, electron charge e, electron mass m_e, and vacuum permittivity ε_o, so that the plasma refractive index ε varies with the variation of n_e.

PMSE are less strong during heating experiments when the electron temperature is artificially increased, and it is suggested that the enhanced electron diffusivity reduces the spatial pattern of the electrons that enters the radar reflective index [*Chilson et al.,* 2000; *Havnes,* 2004]. The basic picture described above implies that electrons are collected on the negatively charged dust, while dust particles in the mesosphere can be neutral or positively charged, the latter especially in nanometer-size limit [*Mann et al.,* 2014]. Also, other processes may play a role, as in their review Rapp and Lübken point out that irregular electron density profiles are frequently observed at PMSE altitudes [*Rapp and Lübken,* 2004]. In some cases charged ice/dust particles are observed at the same time with reduced electron density called "biteout" [*Rapp and Lübken,* 2004; *La Hoz et al.,* 2006]. Aside from local variations observations also indicate the influence of enhanced electron density, e.g., during strong solar proton events on PMSE [*Chau et al.,* 2014]. In view of all this, having electron density and PMSE measurements at the same location and time would be helpful. When using high power large aperture radar like EISCAT for PMSE observations the electron densities can be derived from incoherent scatter at least below and above PMSE. Since the UHF observations that we made simultaneously with the VHF observations show no PMSE, the UHF data could provide electron densities even within PMSE.

The UHF observations presented (Figure 4), however, show no reduced electron densities at PMSE altitude when these are between 85 and 90 km; below 85 km the electron densities are at the detection limit. Instead, both UHF and VHF (Figure 4) seem to indicate from 11 UT onward a reduced electron density between roughly 85 and 90 km altitude directly above the range where PMSE are observed. The observations are, however, close to noise level and not sufficient to decide whether this observed reduced electron density above the PMSE is significant and whether or not it is linked to and a characteristic of PMSE or not.

5. Concluding Remarks

In summer 2013 the EISCAT VHF was for the first time used for tristatic observations, and as far as we know the presented data are among the first undisturbed tristatic PMSE observations over several hours, since most other tristatic observations were made in combination with artificial heating. Because of the large volume illuminated by the radar beam we here can clearly identify the gradients in horizontal motion only in special cases, e.g., through change in direction of the frequency shift. A future multistatic phased-array radar system [*Wannberg et al.,* 2010; *McCrea et al.,* 2015] could provide the opportunity to study the PMSE conditions on smaller spatial scale and solve the space-time ambiguity common to the existing single site atmospheric radars.

References

Andrews, D. G., J. R. Holton, and C. B. Leovy (1987), *Middle Atmosphere Dynamics*, 489 pp., Academic, New York.
Baumann, C., M. Rapp, M. Anttila, A. Kero, and P. T. Verronen (2015), Effects of meteoric smoke particles on the *D* region ion chemistry, *J. Geophys. Res. Space Physics*, 120, 10,823–10,839, doi:10.1002/2015JA021927.
Belova, E., S. Kirkwood, R. Latteck, M. Zecha, H. Pinedo, J. Hedin, and J. Gumbel (2014), Multi-radar observations of polar mesosphere summer echoes during the PHOCUS campaign on 20–22 July 2011, *J. Atmos. Sol. Terr. Phys.*, 118, 199–205, doi:10.1016/j.jastp.2014.06.011.
Chau, J. L., J. Röttger, and M. Rapp (2014), PMSE strength during enhanced D region electron densities: Faraday rotation and absorption effects at VHF frequencies, *J. Atmos. Sol. Terr. Phys.*, 118, 113–118, doi:10.1016/j.jastp.2013.06.015.
Chilson, P. B., E. Belova, M. T. Rietveld, S. Kirkwood, and U.-P. Hoppe (2000), First artificially induced modulation of PMSE using the EISCAT heating facility, *Geophys. Res. Lett.*, 27, 3801–3804, doi:10.1029/2000GL011897.
Cho, J. Y. N., and J. Röttger (1997), An updated review of polar mesosphere summer echoes: Observation, theory, and their relationship to noctilucent clouds and subvisible aerosols, *J. Geophys. Res.*, 102, 2001–2020, doi:10.1029/96JD02030.
Cho, J. Y. N., T. M. Hall, and M. C. Kelley (1992), On the role of charged aerosols in polar mesospheric summer echoes, *J. Geophys. Res.*, 97, 875–886, doi:10.1029/91JD02836.
Dalin, P., S. Kirkwood, M. Hervig, M. Mihalikova, D. Mikhaylova, I. Wolf, and A. Osepian (2012), Wave influence on polar mesosphere summer echoes above Wasa: Experimental and model studies, *Ann. Geophys.*, 30, 1143–1157, doi:10.5194/angeo-30-1143-2012.
Dalin, P. N., S. Pertsev, O. Frandsen, H. Hansen, A. Andersen, R. Dubietis, and R. Balciunas (2010), A case study of the evolution of a Kelvin-Helmholtz wave and turbulence in noctilucent clouds, *J. Atmos. Sol. Terr. Phys.*, 72, 1129–1138, doi:10.1016/j.jastp.2010.06.011.
DeLand, M. T., and G. E. Thomas (2015), Updated PMC trends derived from SBUV data, *J. Geophys. Res. Atmos.*, 120, 2140–2166, doi:10.1002/2014JD022253.

Fritts, D. C., and M. J. Alexander (2003), Gravity wave dynamics and effects in the middle atmosphere, *Rev. Geophys.*, *41*(1), 1003, doi:10.1029/2001RG000106.

Gadsden, M. (1990), A secular change in noctilucent cloud occurrence, *J. Atmos. Solar Terr. Phys.*, *52*, 247–251.

Havnes, O. (2004), Polar Mesospheric Summer Echoes (PMSE) overshoot effect due to cycling of artificial electron heating, *J. Geophys. Res.*, *109*, A02309, doi:10.1029/2003JA010159.

Havnes, O., J. Trøim, T. Blix, W. Mortensen, L. I. Næsheim, E. Thrane, and T. Tønnesen (1996), First detection of charged dust particles in the Earth's mesosphere, *J. Geophys. Res.*, *101*, 10,839–10,848, doi:10.1029/96JA00003.

Hervig, M. E., D. E. Siskind, M. H. Stevens, and L. E. Deaver (2013), Inter-hemispheric comparison of PMCs and their environment from SOFIE observations, *J. Atmos. Sol. Terr. Phys.*, *104*, 285–298, doi:10.1016/j.jastp.2012.10.013.

Hill, R. J. (1978), Nonneutral and quasi-neutral diffusion of weakly ionized multiconstituent plasma, *J. Geophys. Res.*, *83*, 989–998, doi:10.1029/JA083iA03p00989.

Hill, R. J., D. E. Gibson-Wilde, J. A. Werne, and D. C. Fritts (1999), Turbulence-induced fluctuations in ionization and application to PMSE, *Earth Planets Space*, *51*, 499–513, doi:10.1186/BF03353211.

Hysell, D. L., J. Munk, and M. McCarrick (2014), Sporadic E ionization layers observed with radar imaging and ionospheric modification, *Geophys. Res. Lett.*, *41*, 6987–6993, doi:10.1002/2014GL061691.

Kirkwood, S., J. Cho, C. M. Hall, U.-P. Hoppe, D. P. Murtagh, J. Stegman, W. E. Swartz, A. P. van Eyken, G. Wannbergt, and G. Witt (1995), A comparison of PMSE and other ground-based observations during the NLC-91 campaign, *J. Atmos. Sol. Terr. Phys.*, *57*, 35–44, doi:10.1016/0021-9169(93)E0032-5.

La Hoz, C., O. Havnes, L. I. Næsheim, and D. L. Hysell (2006), Observations and theories of Polar Mesospheric Summer Echoes at a Bragg wavelength of 16 cm, *J. Geophys. Res.*, *111*, D04203, doi:10.1029/2005JD006044.

Lehtinen, M. S., and A. Huuskonen (1996), General incoherent scatter analysis and GUISDAP, *J. Atmos. Sol. Terr. Phys.*, *58*, 435–452, doi:10.1016/0021-9169(95)00047-X.

Lübken, F. J., M. Rapp, and P. Hoffmann (2002), Neutral air turbulence and temperatures in the vicinity of polar mesosphere summer echoes, *J. Geophys. Res.*, *107*(D15), 4273, doi:10.1029/2001JD000915.

Mann, I., N. Meyer-Vernet, and A. Czechowski (2014), Dust in the planetary system: Dust interactions in space plasmas of the solar system, *Phys. Rep.*, *536*, 1–39, doi:10.1016/j.physrep.2013.11.001.

McCrea, I., et al. (2015), The science case for the EISCAT_3D radar, *Prog. Earth Planet. Sci.*, *2*, 21, doi:10.1186/s40645-015-0051-8.

Megner, L., and J. Gumbel (2009), Charged meteoric particles as ice nuclei in the mesosphere: Part 2. A feasibility study, *J. Atmos. Sol. Terr. Phys.*, *71*, 1236–1244, doi:10.1016/j.jastp.2009.05.002.

Mendis, D. A., and M. Rosenberg (1994), Cosmic dusty plasmas, *Annu. Rev. Astron. Astrophys.*, *32*, 419–463, doi:10.1146/annurev.aa.32.090194.002223.

Morris, R. J., D. J. Murphy, A. R. Klekociuk, and D. A. Holdsworth (2007), First complete season of PMSE observations above Davis, Antarctica, and their relation to winds and temperatures, *Geophys. Res. Lett.*, *34*, L05805, doi:10.1029/2006GL028641.

Nussbaumer, V., K. H. Fricke, M. Langer, W. Singer, and U. von Zahn (1996), First simultaneous and common volume observations of noctilucent clouds and polar mesosphere summer echoes by lidar and radar, *J. Geophys. Res.*, *101*, 19,161–19,167, doi:10.1029/96JD01213.

Pertsev, N., P. Dalin, V. Perminov, V. Romejko, A. Dubietis, R. Balčiunas, K. Černis, and M. Zalcik (2014), Noctilucent clouds observed from the ground: Sensitivity to mesospheric parameters and long-term time series, *Earth Planets Space*, *66*, 98, doi:10.1186/1880-5981-66-98.

Plane, J. M. C., W. Feng, and E. C. M. Dawkins (2015), The mesosphere and metals: Chemistry and changes, *Chem. Rev.*, *115*, 4497–4541, doi:10.1021/cr500501m.

Rapp, M., and F. J. Lübken (2004), Polar mesosphere summer echoes (PMSE): Review of observations and current understanding, *Atmos. Chem. Phys. Discuss.*, *4*, 4777–4876, doi:10.5194/acpd-4-4777-2004.

Rapp, M., and F. J. Lübken (2009), Comment on "Ice iron/sodium film as cause for high noctilucent cloud radar reflectivity" by P. M. Bellan, *J. Geophys. Res.*, *114*, D11204, doi:10.1029/2008JD011323.

Remsberg, E. E., et al. (2008), Assessment of the quality of the Version 1.07 temperature-versus-pressure profiles of the middle atmosphere from TIMED/SABER, *J. Geophys. Res.*, *113*, D17101, doi:10.1029/2008JD010013.

Röttger, J., and C. LaHoz (1990), Characteristics of polar mesosphere summer echoes (PMSE) observed with the EISCAT 224 MHz radar and possible explanations of their origin, *J. Atmos. Terr. Phys.*, *52*, 893–906, doi:10.1016/0021-9169(90)90023-G.

Russell, J. M., III, M. G. Mlynczak, L. L. Gordley, J. Tansock, and R. Esplin (1999), An overview of the SABER experiment and preliminary calibration results, *Proc. SPIE Int. Soc. Opt. Eng.*, *3756*, 277–288.

Strelnikova, I., and M. Rapp (2010), Studies of polar mesospheric summer echoes with EISCAT VHF and UHF radars: Information contained in the spectral shape, *Adv. Space Res.*, *45*, 247–259, doi:10.1016/j.asr.2009.09.007.

Strelnikova, I., and M. Rapp (2011), Majority of PMSE spectral widths at UHF and VHF are compatible with a single scattering mechanism, *J. Atmos. Sol. Terr. Phys.*, *73*, 2142–2152, doi:10.1016/j.jastp.2010.11.025.

Thomas, G. E. (2003), Are noctilucent clouds harbingers of global change in the middle atmosphere? *Adv. Space Res.*, *32*, 1737–1746, doi:10.1016/S0273-1177(03)90470-4.

Thomas, G. E., J. J. Olivero, E. J. Jensen, W. Schröder, and O. B. Toon (1989), Relation between increasing methane and the presence of ice clouds at the mesopause, *Nature*, *338*, 490–492, doi:10.1038/338490a0.

Varney, R. H., M. C. Kelley, M. J. Nicolls, C. J. Heinselman, and R. L. Collins (2011), The electron density dependence of polar mesospheric summer echoes, *J. Atmos. Sol. Terr. Phys.*, *73*, 2153–2165, doi:10.1016/j.jastp.2010.07.020.

von Zahn, U. (2003), Are noctilucent clouds truly a "miner's canary" of global change? *Eos Trans. AGU*, *84*(28), 261–268, doi:10.1029/2003EO280001.

Wannberg, U. G., et al. (2010), EISCAT_3D—A next-generation European radar system for upper atmosphere and geospace research, *Radio Sci. Bull.*, *332*, 75–88.

Yu, T. Y., R. D. Palmer, and P. B. Chilson (2001), An investigation of scattering mechanisms and dynamics in PMSE using coherent radar imaging, *J. Atmos. Terr. Phys.*, *63*(17), 1797–1810, doi:10.1016/S1364-6826(01)00058-X.